IEEE Access
Multidisciplinary | Rapid Review | Open Access Journal

Received 4 July 2024, accepted 30 July 2024, date of publication 2 August 2024, date of current version 12 August 2024.

Digital Object Identifier 10.1109/ACCESS.2024.3437473

RESEARCH ARTICLE

Dual-Polarized Patch Antenna Array Integrated With Capacitive Proximity Sensor for 5G Millimeter-Wave Smartphones

JEONG-UNG YOO, JUNG-MU KIM, (Member, IEEE), DONGGU IM, (Member, IEEE), AND HAE-WON SON, (Member, IEEE)

Division of Electronics and Information Engineering, Jeonbuk National University, Jeonju 54896, South Korea

Corresponding author: Hae-Won Son (hwson@jbnu.ac.kr)

This work was supported by the National Research Foundation of Korea (NRF) Grant funded by the Korea Government (MSIT) under Grant RS-2024-00399396.

ABSTRACT We present a novel concept of a millimeter-wave patch antenna that integrates the functions of a dual-polarized antenna and a capacitive proximity sensor to detect the state of a hand grip on a smartphone and compensate for the effect. The antenna has a dual-polarized, proximity-coupled, square patch structure, and acts as a proximity sensor by utilizing the change in capacitance of the patch when the user's hand approaches. By observing the change in capacitance at the center of a square patch operating in two fundamental TM modes, antenna and sensor functions can be performed concurrently and without mutual interference. The antenna is designed using a low-cost four-layer FR-4 substrate and fabricated using a cost-effective standard printed circuit board (PCB) process. The antenna is configured as a 1×8 array, and after mounting it on a smartphone model, the gain, beam steering performance, and change in capacitance according to hand proximity are predicted and measured. The peak gain measured at 28 GHz exceeds 11.8 dBi, with a gain variation of less than 2.2 dB within the 5 G 257 band ($26.5 - 29.5$GHz). The measured capacitance change due to hand proximity is 130 fF, which is sufficient for real-time detection of the hand grip state. An example of improvement in the gain of the proposed antenna by detecting the hand grip state is presented through a simulation.

INDEX TERMS 5G, capacitive proximity sensor, dual-polarization, hand effect, millimeter-wave (mmWave), patch antenna, phased array antenna.

I. INTRODUCTION

Millimeter wave (mmWave) 5G communications are expected to play an important role in managing the rapidly increasing volumes of traffic from mobile devices by providing high data rates across a wide available bandwidth [1], [2]. In the mmWave band, high-gain phased array antennas are used in base stations and mobile terminals to mitigate degradation in performance of wireless communication systems caused by high path loss. Thanks to extensive research on efficient semiconductor circuits and antennas, significant advancements have been achieved in commercializing fixed mmWave systems such as base stations and wireless backhauls, which face no major constraints on the space occupied by the antenna and the environment in which it operates [3], [4], [5], [6]. However, for mobile terminals, especially smartphones, which have limited internal space and must operate in diverse user environments, antenna design must take into account the significant difficulties posed by size, performance, price, and the various hand grip patterns of users [7], [8], [9].

Mobile antennas in the mmWave band are manufactured using primarily multilayer printed circuit board (PCB) technology and are designed to radiate predominantly in the lateral direction of the smartphone [9], [10], [11], [12], [13], [14], [15], [16], [17], [18], [19], [20]. This is an appropriate

The associate editor coordinating the review of this manuscript and approving it for publication was Zahra Shaterian.

choice given the interference from the display and battery and the effect of the user's hands. Various mmWave mobile phased array antennas have been introduced in which linearly polarized radiators based on patches [9], [10], dipoles [11], [12], [13], [14], and slots [15], [16] are arranged in a row at the edge of a thin multilayer PCB, enabling beams to be steered along the side of the PCB. These antennas are manufactured as modules and mounted on the main PCB of the smartphone [14], [15], [16] or integrated directly into the main PCB [10], [12], greatly reducing the space they occupy inside the smartphone. Other types of array antennas have been proposed to facilitate beam steering along the side of a smartphone. These include a structure in which planar broadside radiators (e.g., patches and slots) are arranged in a row on a narrow, long PCB [17], [18], [19], [20] and mounted parallel to the side of a smartphone. They are produced as independent modules [17], [18], [19] or as integrated elements that match the shape of the smartphone case [20].

To enable independent development of smartphones and antennas and to allow for various compatible combinations between them, phased array antennas in the form of antenna-in-package (AiP) modules are required. AiP modules can be fabricated using various dielectric substrates, including low temperature co-fired ceramic (LTCC), polytetrafluoroethylene (PTFE), and FR-4 epoxy laminates. In the mmWave band, LTCC and PTFE are preferred because they have low loss and allow for fine wiring, but require expensive materials and processing. FR-4 substrates, by comparison, are associated with a high dielectric loss but a low price, and the standard PCB process for mass production is well developed, making the manufacturing costs low. Various mmWave antennas using FR-4 substrates have been studied [21], [22], [23].

Meanwhile, the performance of mobile antennas in the mmWave band can be significantly degraded due to interference from the user's hands [24], [25], [26]. If the user's hands cover some elements of the phased array antenna while holding the smartphone, the signal radiating from those covered elements can be blocked, reducing the gain of the array antenna or making it impossible to steer the main beam in the desired direction. Solving this problem requires installing hand detection sensors around each element, analyzing the user's hand grip states in real time, and controlling the amplitude and phase of the radio frequency (RF) signal supplied to each element to maintain optimal overall array performance. In [25], a method has been proposed to optimize the array antenna's performance according to the user's hand grip pattern by creating a beamforming codebook, but no specific device capable of detecting hand grip patterns in real time was presented.

Recently, we introduced a new concept of a patch antenna that integrates the functions of an antenna and a capacitive proximity sensor, and presented a phased array antenna based on it [18], [19], [27]. We called this device a "sentenna (sensor + antenna)." Fig. 1 is a schematic of the hand effect

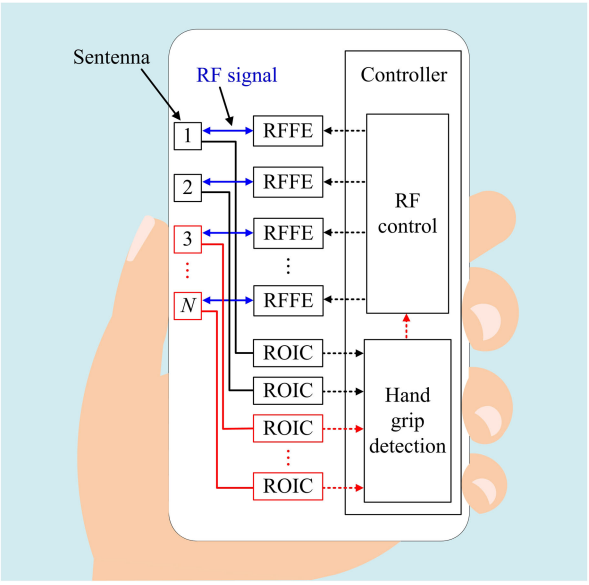

FIGURE 1. Sentenna-based hand effect compensation system for a 5G mmWave smartphone.

compensation system, comprising a $1 \times N$ sentenna array (SA), readout integrated circuits (ROICs), RF front ends (RFFEs), and a controller. In this system, the SA radiates mmWave RF signals and is simultaneously connected to ROICs to monitor capacitance changes and detect hand grip states in real time. If certain sentenna elements (SEs) are not radiating effectively due to hand interference, the controller adjusts the amplitude and phase of the RF signal supplied to each SE to optimize the performance of the entire SA. For example, the gain of the overall SA can be improved by halting the signal supplied to the SEs obscured by the hand and redistributing the signal power to other SEs.

In this paper, we propose a 1×8 dual-polarized SA by expanding on our previous works [18], [19]. We elaborate on the structure of a dual-polarized SE, along with the underlying mechanism of how a single patch can act simultaneously as a wideband radiator and a capacitive sensor without mutual interference. After mounting the proposed SA on a smartphone model, we predict antenna gain, beam steering performance, and capacitance change according to hand proximity through a simulation and verify the results in experiments. Finally, a specific example illustrating the improvement in SA gain when a portion of the proposed SA is obscured by a hand is explained through simulations. This paper focuses on implementing and validating the antenna and sensor functions of the proposed sentenna and does not address the ROIC, RFFE, or controller.

II. SENTENNA DESIGN

A. SENTENNA CONFIGURATION

Fig. 2(a) depicts the geometry of the proposed sentenna. The sentenna has a basic structure of a dual-polarized, proximity-coupled, square patch antenna and is designed on a four-layer PCB consisting of one core and two prepregs.

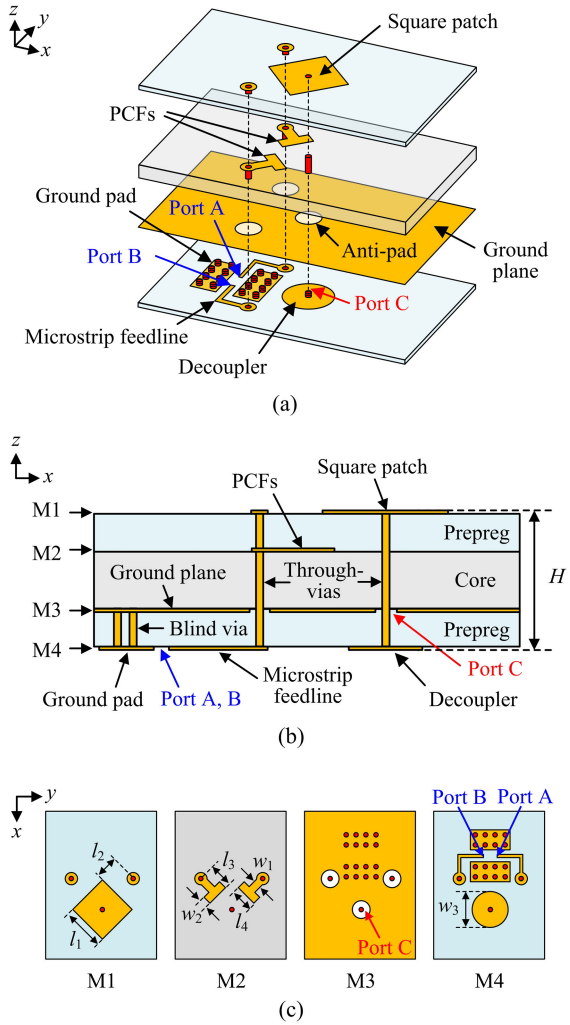

FIGURE 2. Geometry of the proposed sentenna. (a) Three-dimensional view. (b) Rough side view. (c) Top view of the four metal layers.

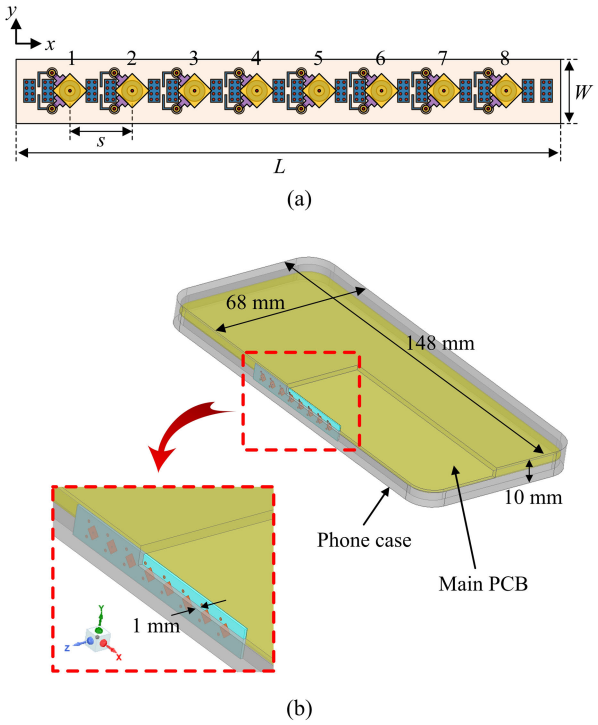

FIGURE 3. 1 × 8 SA. (a) Top view. (b) Side-mounted view into a smartphone.

TABLE 1. Dimensions of the SE and SA.

Parameter	l_1	l_2	l_3	l_4	w_1	w_2
Value (mm)	2.1	1.1	1.2	1.1	0.4	0.4
Parameter	w_3	s	L	W	H	
Value (mm)	1.8	5.4	48	6	0.61	

Both the core and prepregs are FR-4 ($\varepsilon_r = 4.1$, $\tan\delta = 0.03$), and the sentenna is fabricated using a cost-effective PCB process. A schematic side view of the sentenna, illustrating four metal layers (M1, M2, M3, and M4) and the vias between them, is presented in Fig. 2(b). The sentenna uses a proximity-coupled feed (PCF) structure to achieve wideband characteristics covering the entire 5G n257 band (26.5 − 29.5 GHz). A square patch, two PCFs, and a ground plane are printed on the M1, M2, and M3 layers, respectively. To attain slanted ±45° dual polarization, a square patch is positioned at a 45° angle, and two T-shaped PCFs are arranged orthogonally in the −45° and +45° directions, respectively.

On the M4 layer, two microstrip feedlines are printed and connected to their corresponding PCFs by through-vias from the M1 to M4 layers. Two antenna ports (ports A and B) are located at the ends of the feedlines. Port A excites the −45° polarization, and port B excites the +45° polarization. In a realistic AiP module using the proposed sentenna, the RFFE and ROIC may be mounted on the M4 layer. However, as neither the RFFE nor the ROIC is within the scope of this paper, a temporary structure to connect the evaluation feed boards (described in Section IV) is placed on the M4 layer instead. In this regard, on the M4 layer, two ground pads (connected by blind vias to the ground plane of the M3 layer) are formed and arranged around the antenna ports. Fig. 2(c) provides a top view of each metal layer of the sentenna.

In the proposed sentenna design, the square patch is connected to the sensor port (port C in Fig. 2) through a central through-via. This connection allows the patch to function as an electrode for a capacitive proximity sensor while maintaining its properties as an antenna. The sensor port is defined across the anti-pad of the central via, which is the void area between the via and the ground plane in the M3 layer. The via connects to the center of the circular stub in the M4 layer, labeled a ‘‘decoupler’’ in the figure. The decoupler functions as a zero-impedance resonator connected in parallel to the sensor port, preventing the mmWave antenna signal from leaking into the sensor port.

Using the proposed sentenna, we constructed a 1 × 8 SA, as shown in Fig. 3(a). Patches and feed structures for both polarizations are arranged symmetrically about the axis plane (xz-plane) of the array. Therefore, the radiation patterns of

the two polarized waves are symmetrical with respect to the *xz*-plane, which is the beam steering plane of the phased array sentenna. The spacing (s) between SEs is 5.4 mm, corresponding to a half-wavelength in free space at 28 GHz. The overall SA size is 48 mm × 6 mm × 0.61 mm. Detailed dimensions of the SE and SA are listed in Table 1. The diameters of the through-vias and blind vias are 0.3 mm and 0.2 mm, respectively. These via diameters are typical minimums for low-cost standard PCB processes. All metal layers are 0.017 mm thick copper. The core is 0.4 mm thick, and the prepreg style is 1080 with a thickness of 0.076 mm. Fig. 3(b) shows the SA mounted on a smartphone model. The SA design assumes that it will be mounted on the side of a smartphone, as shown in the figure. At this time, the square patch of the sentenna adheres closely to the plastic case of the smartphone. The plastic case not only affects the sentenna's antenna characteristics but also limits the minimum distance between the user's hand and the square patch to at least the thickness of the case when operating as a proximity sensor. Given this situation, the sentenna design assumes it is covered with a plastic case made of acrylonitrile butadiene styrene (ABS), with a thickness of 1 mm ($\varepsilon_r = 2.8$, $\tan\delta = 0.005$).

B. ANTENNA-TO-SENSOR ISOLATION

In the sentenna, the patch can function both as an antenna radiator and as an electrode for a capacitive proximity sensor. As the user's hand approaches the patch, the mutual capacitance between the patch and the ground plane changes. By observing this change, it is possible to determine how close the user's hand is to the patch. However, to use one patch simultaneously as both an antenna and a sensor electrode, a high level of isolation is required to ensure their independent operations. Fortunately, because the antenna operates in the mmWave band and the frequency of the test signal for the capacitive sensor can be as low as 1 MHz, it can be designed with high isolation in each operating frequency band.

The square patch has a half-wavelength in the mmWave band and operates at the fundamental TM_Z mode. Fig. 4(a) depicts the distribution of the electric field under the patch at the fundamental TM_z mode in the resonant length direction. The length of the arrow indicates the amplitude of the electric field. The distribution of the electric field is maximal at both ends of the patch and null at the center of the patch. By connecting a thin probe at this null position to the patch, the capacitance of the patch can be measured without degrading its radiation characteristics. For this reason, a via connecting the patch and the sensor port is located at the center of the patch, as shown in Fig. 2.

Meanwhile, the patch is fed by proximity coupling in the mmWave band. This approach not only enhances the antenna bandwidth but prevents the sensor test signal from leaking into the antenna port. Fig. 4(b) illustrates the equivalent capacitance (C_e) between the patch and the PCF. In the mmWave band, C_e exhibits low impedance, allowing the antenna signal to flow. However, at the low frequency of the sensor test signal, the high impedance of C_e blocks the test signal. The sensor characteristics are therefore not affected significantly by the condition of the antenna port.

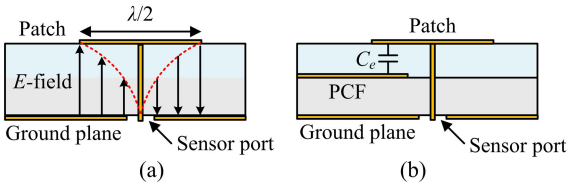

FIGURE 4. (a) Electric field distribution under the patch. (b) Equivalent capacitance (C_e) between the patch and the PCF.

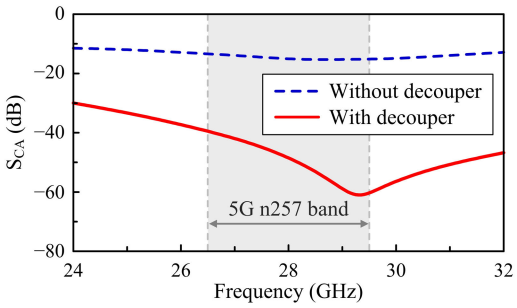

FIGURE 5. Simulated isolation between the antenna port (port A) and the sensor port (port C) of the sentenna with and without a decoupler.

C. ENHANCING ISOLATION USING A DECOUPLER

Because capacitance sensing is conducted at the center of the patch, a high degree of isolation between the antenna and sensor ports can be expected. However, the large anti-pad formed on the ground plane beneath the patch for the sensor port can significantly degrade the isolation. When using a cost-effective standard PCB process, the anti-pad must be at least 0.5 mm in diameter, which is too large to be ignored in the mmWave band. The distribution of the electric field of the TM_Z resonance mode under the patch is disturbed by the anti-pad, resulting in the signal leaking into the sensor port.

Fig. 5 depicts the simulated isolation between the antenna and sensor ports (for a 50-ohm reference impedance). Isolation is as low as 15 dB or less in the 5G n257 band. To address this, a circular stub-type decoupler is designed and connected in parallel to the sensor port. The decoupler is printed on the M4 layer and connected with a via in the center, completely covering the anti-pad. The decoupler is an open-stub resonator with zero impedance at its center. Therefore, signal leakage to the sensor port is blocked by shorting the sensor port in the mmWave band. Fig. 5 also shows the simulated isolation with the decoupler installed. With the decoupler, the isolation increases to more than 39 dB in the 5G n257 band, an improvement of more than 24 dB. The condition of the sensor port therefore has little effect on the antenna characteristics in the mmWave band.

III. SIMULATION RESULTS

A. ANTENNA CHARACTERISTICS

The antenna-related performance of the proposed sentenna is simulated using Ansys HFSS. We first describe the radiation

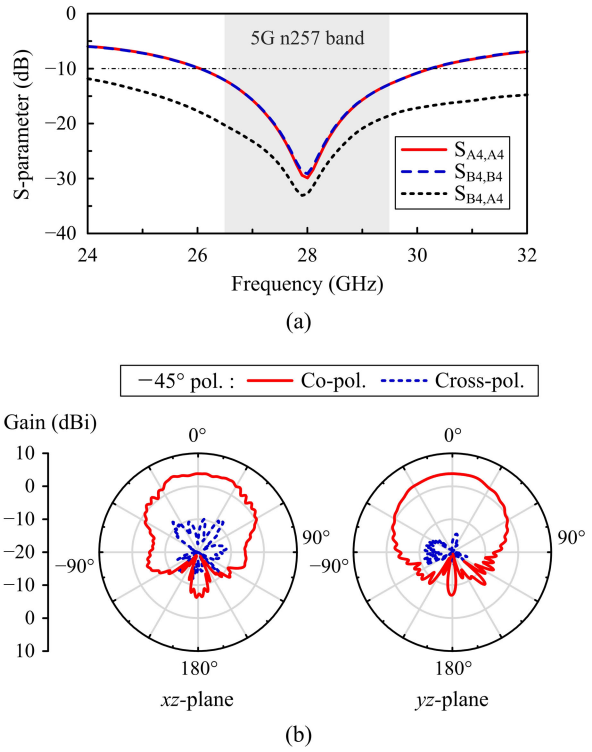

FIGURE 6. Simulated antenna performance of the SE 4. (a) S-parameters. (b) Radiation pattern at 28 GHz (−45° polarization).

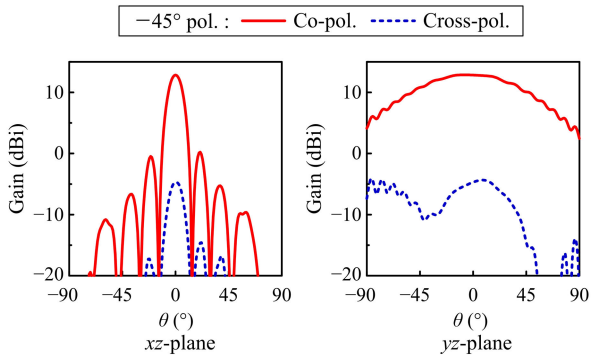

FIGURE 7. Simulated radiation pattern of the SA for $\theta_s = 0°$ at 28 GHz (−45° polarization).

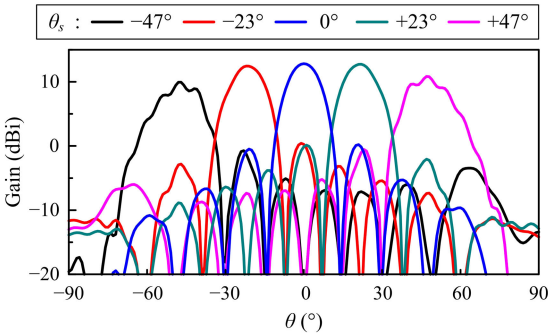

FIGURE 8. Simulated beam steering radiation patterns of the SA in the *xz*-plane at 28 GHz (−45° polarization).

properties of the SE and then those of the SA. Fig. 6(a) shows the simulated S-parameters of the SE 4, with element numbers indicated in Fig. 3(a). The antenna ports of the SE 4 are labeled A4 (−45° polarization) and B4 (+45° polarization). The 10-dB return loss bandwidth (RLBW) of both ports is 14.6% (26.1 to 30.2 GHz), covering the 5G n257 band. Isolation between the two ports exceeds 19 dB within this band. Fig. 6(b) displays the simulated radiation pattern for the −45° polarization of the SE 4 in two orthogonal planes (*xz*- and *yz*-planes, which are the diagonal planes of the square patch) at 28 GHz. The SE exhibits a gain of 3.8 dBi in the broadside direction, with a half-power beamwidth (HPBW) of 92° and 105° in the *xz*- and *yz*-planes, respectively. The cross-polarization is lower than −12 dB within the HPBW. Due to the symmetrical structure of the sentenna, the radiation pattern of the +45° polarization is symmetrical to that of the −45° polarization with respect to the *xz*-plane, but for brevity is not shown here.

Fig. 7 depicts the simulated radiation patterns for the −45° polarization of the 1 × 8 SA at 28 GHz. All SEs are fed with the same amplitude and phase, and the main beam is in the broadside direction (i.e., steering angle of $\theta_s = 0°$). The peak gain is 12.8 dBi, with an HPBW of 12° and 101° in the *xz*- and *yz*-planes, respectively. The cross-polarization is less than −17 dB in the main beam.

The main beam of the SA can be steered in different directions through different phase excitations. Fig. 8 illustrates the simulated radiation patterns when the main beam is steered at $\theta_s = 0°$, ±23°, and ±47° for the −45° polarization in the *xz*-plane. There is a gain variation of 2.9 dB within this steering range. The radiation patterns exhibit ripples, particularly for $\theta_s = \pm 47°$. These ripples are mainly caused by surface waves propagating along the smartphone case. In Fig. 3(b), the main PCB, the plastic case, and the air gap between them form a multilayer structure that guides these surface waves. These surface waves interfere with the direct radiation from the sentenna, resulting in the observed ripples in the far-field pattern. Further simulations confirmed that the ripples disappear when the plastic case is removed. The simulated beam steering radiation patterns for the +45° polarization are identical to those for the −45° polarization in the *xz*-plane but for clarity are not shown here.

B. SENSOR CHARACTERISTICS

The sensor function is based on measuring the change in capacitance when the user's hand is or is not positioned on the sentenna (more precisely, when the hand touches or moves away from the plastic case covering the sentenna). In this paper, the sensor performance is simulated using Ansys Q3D Extractor. Fig. 9(a) depicts the simulation setup used to simulate the capacitance change of a sentenna at the sensor port. Instead of a human hand, we simulated the capacitance change of the SE 4 by bringing a small, grounded metal plate (15 mm × 30 mm size) close to the SE. This was done to obtain consistent data in a controlled experimental environment. A grounded metal plate is a useful approximate model of the human hand (or fingers) because the human

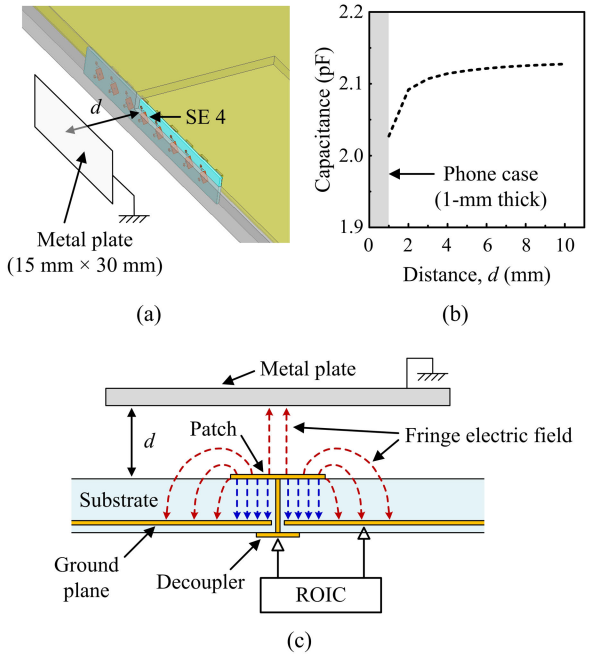

FIGURE 9. Simulated capacitance change of the sentenna according to the sentenna-to-metal plate distance (d). (a) Simulation setup. (b) Capacitance change. (c) Illustration of the principle behind the capacitance change.

body, being relatively large and having high capacitance, is typically considered to be at zero electric potential in the analysis and design of the capacitive proximity sensors based on fringing capacitance [28], [29]. Fig. 9(b) shows the capacitance change of the sentenna against the distance (d) between the sentenna and the metal plate (observed between the square patch of the SE 4 and the ground plane) at a test frequency of 1 MHz. When $d = 1$ mm, the metal plate touches the plastic case over the sentenna. As the metal plate approaches the sentenna, the capacitance decreases, which is a typical response of capacitive proximity sensors utilizing fringing capacitance [28]. Fig. 9(c) illustrates the principle behind this capacitance decrease. Initially, when a potential difference is applied between the patch and the ground plane, an electric field is formed between them. Most of the field is concentrated within the substrate region between the patch and the ground plane. However, a fringe electric field extends from the patch, out of the substrate, and returns to the ground plane. When a grounded metal plate is brought close to the patch, the fringe field is disrupted, and a portion of the electric field is redirected to the metal plate instead of the ground plane. Consequently, the mutual capacitance between the patch and the ground plane decreases, which is detected by the ROIC.

In Fig. 9(b), the capacitance decreases slowly as the metal plate approaches the sentenna, then decreases rapidly when the metal plate touches the case. When the metal plate is far from the sentenna, the capacitance is 2.127 pF, and when the metal plate touches the case over the sentenna, it decreases to 2.027 pF. This indicates that the capacitance decreases

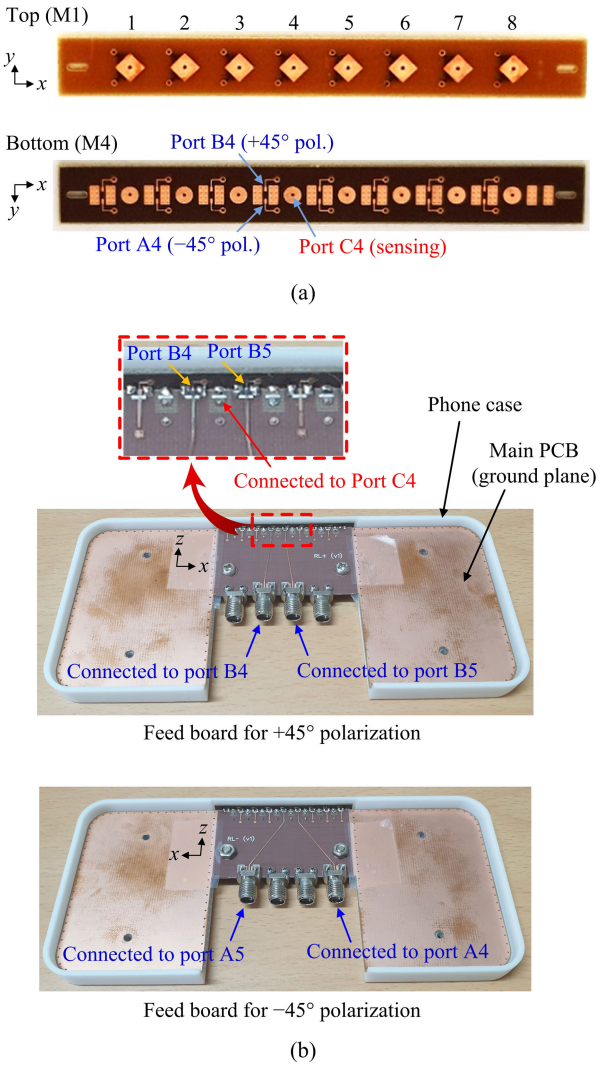

FIGURE 10. Photographs of the prototype sentenna. (a) Top and bottom views of the SA. (b) SA mounted on a smartphone with a pair of feed boards to test the SE 4.

by approximately 100 fF when the grounded metal plate is placed near the sentenna, demonstrating that the proposed sentenna can function effectively as a capacitive proximity sensor. Similar results are expected when a real human hand is brought close to the sentenna, which will be described in detail in Section IV-B.

IV. EXPERIMENTAL VERIFICATION

A prototype of the proposed SA was fabricated as shown in Fig. 10(a). The prototype is too small to measure by directly attaching regular RF connectors. Therefore, we designed separate feed boards and attached them vertically to the SA. Fig. 10(b) shows a pair of feed boards used to measure the performance of SEs 4 and 5. These feed boards are designed for the −45° and +45° polarization feeds, respectively, and are attached vertically to an SA with their ground planes facing each other. The ground planes of both feed boards are connected to the ground plane of the main PCB of the

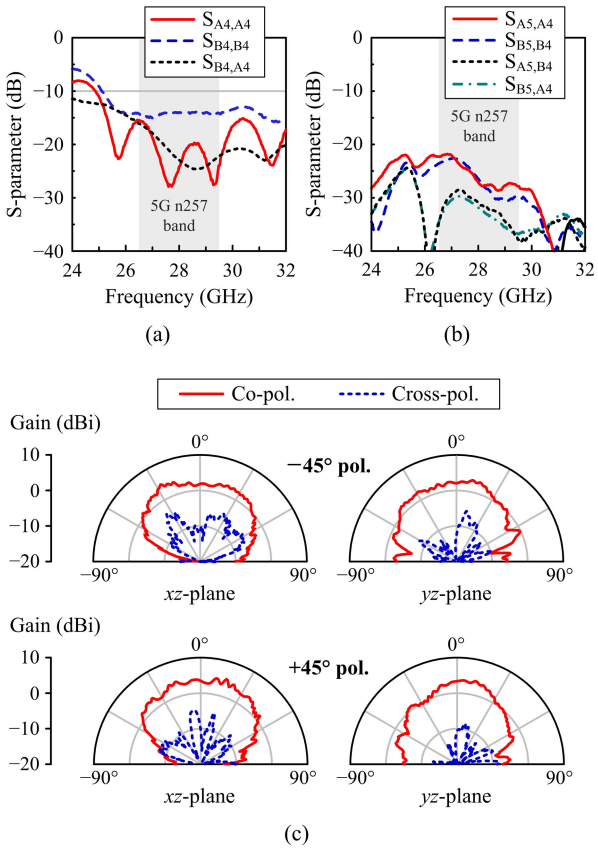

FIGURE 11. Measured antenna performance of the SE 4. (a) S-parameters, (b) Isolations between adjacent SEs. (c) Radiation patterns at 28 GHz.

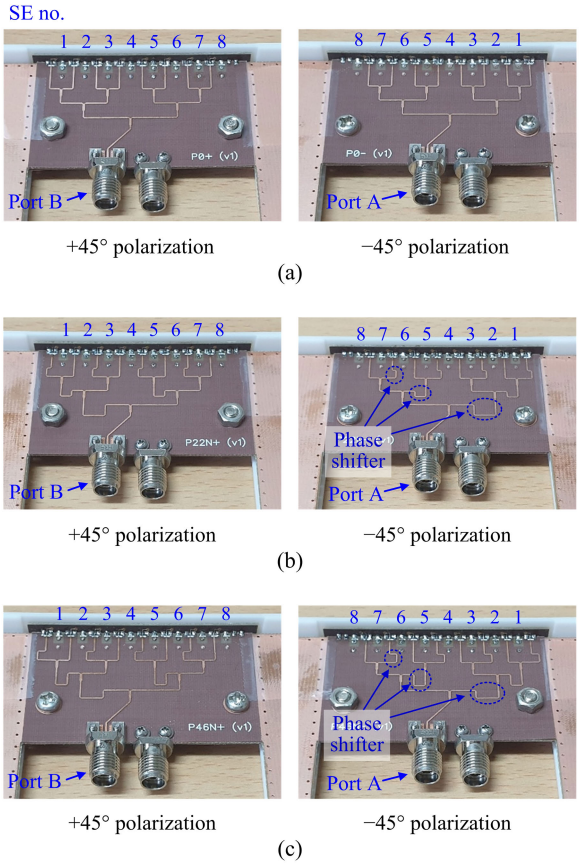

FIGURE 12. BSNs to test the SA. (a) BSN 1 ($\theta_s = 0°$). (b) BSN 2 ($\theta_s = 23°$). (c) BSN 3 ($\theta_s = 47°$).

smartphone. The feed board for the −45° polarization has two microstrip lines connected to antenna ports A4 and A5, while the feed board for the +45° polarization has two microstrip lines connected to antenna ports B4 and B5. A 2.92 mm RF connector is connected to each microstrip line. The feed boards are made of a thin Taconic TLY-5 substrate (0.127 mm thick), and a main PCB of a smartphone is made of an FR-4 substrate (0.4 mm thick) with copper ground planes on both sides.

A. ANTENNA CHARACTERISTICS

Fig. 11(a) depicts the measured S-parameters for antenna ports A4 and B4 of the SE 4. Both ports exhibit a return loss of more than 14 dB in the 5G n257 band. The measured 10-dB RLBW is greater than 24% for both ports, which is wider than the simulated bandwidth in Fig. 6(a). This discrepancy is attributable primarily to the insertion loss of approximately 1.0 dB of the microstrip feedlines on the feed board. The measured isolation between the two antenna ports is greater than 16 dB in the 5G n257 band. Fig. 11(b) shows the measured isolations between the adjacent SEs 4 and 5. In the 5G n257 band, the isolation exceeds 22 dB for the same polarization and 29 dB for orthogonal polarization. Consequently, the proposed SE demonstrates sufficient performance to enable construction of a phased array with polarization diversity for 5G applications. Fig. 11(c) shows the measured radiation patterns of the SE 4 at 28 GHz. The measured gains, corrected for the insertion loss of the feed board, are 4.3 dBi and 5.0 dBi for the −45° and +45° polarizations, respectively. The measured cross-polarization is less than −8 dB within the HPBW for both polarizations. Given the influence of the feed boards and test cables, the measured S-parameters and radiation patterns of the SE are in close agreement with the simulation results.

An actual AiP module using the proposed sentenna will incorporate RFFEs, including tunable phase shifters. However, this paper does not address the design of the RFFE. Instead, to verify the gain and beam steering performance of the proposed SA, several beam steering networks (BSNs) with different steering angles were designed and fabricated on the feed board and connected to the SA, as depicted in Fig. 12. BSN 1 in Fig. 12(a) is a 1:8 corporate feed network that supplies signals of equal amplitude and phase to all SEs, resulting in $\theta_s = 0°$. In contrast, BSN 2 and BSN 3 in Figs. 12(b) and 12(c) supply SEs 1 to 8 with signals having sequential phase shifts of −67.5° and −135°, respectively, resulting in $\theta_s = 23°$ and 47°. Additionally, BSNs with $\theta_s = -23°$ and −47° were designed and fabricated, but they are omitted from the figure for simplicity. All BSNs were fabricated using the same substrate as the feed board for the

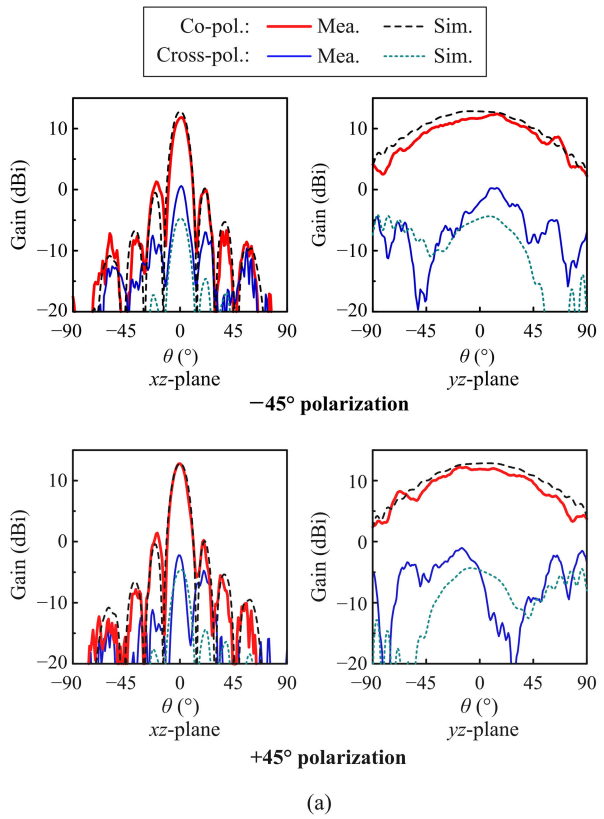

(a)

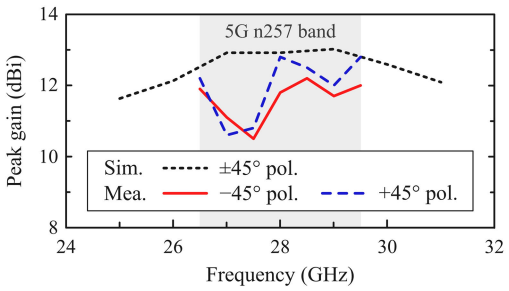

(b)

FIGURE 13. Measured radiation patterns and gain of the SA. (a) Radiation pattern at 28 GHz. (b) Peak gain versus frequency.

SE in Fig. 10(b) and have an insertion loss of approximately 1.7 dB; all measured gains of the SA are corrected for this insertion loss.

Fig. 13 shows the measured radiation performance of the SA for $\theta_s = 0°$ and compares it with simulations. The radiation patterns for the $-45°$ and $+45°$ polarizations at 28 GHz are depicted in Fig. 13(a). The radiation pattern is nearly identical for both polarizations, with peak gains of 11.8 dBi and 12.8 dBi for the $-45°$ and $+45°$ polarizations, respectively. The HPBW is 11° in the *xz*-plane and 90° in the *yz*-plane for both polarizations. The cross-polarization within the main beam is less than -12 dB and -15 dB for the $-45°$ and $+45°$ polarizations, respectively. Fig. 13(b) depicts the measured gain variation of the SA across frequency. In the 5G n257 band, the gain variation is less than 1.7 dB and

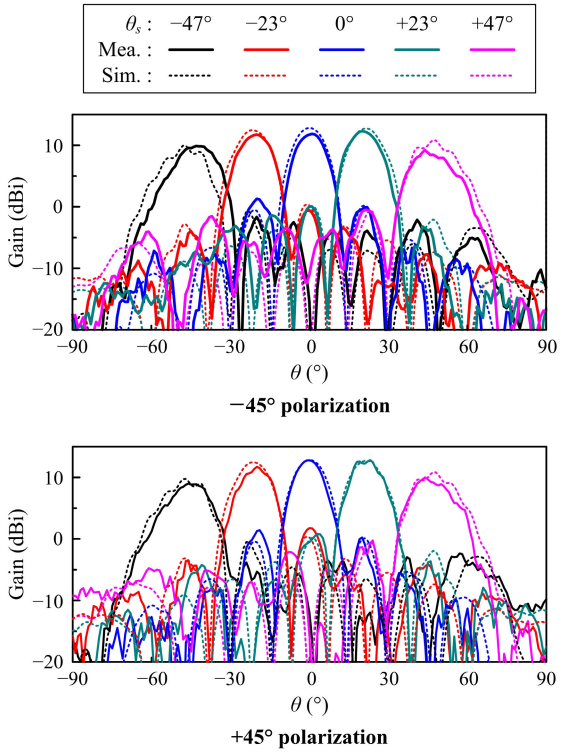

FIGURE 14. Measured beam steering radiation patterns of the SA in the *xz*-plane at 28 GHz.

2.2 dB for the $-45°$ and $+45°$ polarizations, respectively. The measured results are in close agreement with the simulations.

Fig. 14 shows the measured beam steering radiation patterns of the SA for $\theta_s = 0°, \pm 23°$, and $\pm 47°$ and compares them with the simulations. The measured results are in close agreement with the simulations. For the $-45°$ polarization, the measured steering range is from $-43°$ to 44°, with a gain variation of 2.6 dB. For the $+45°$ polarization, the measured steering range is from $-46°$ to 44°, with a gain variation of 3.8 dB. Throughout the steering range, the cross-polarization is less than -8 dB and -12 dB for the $-45°$ and $+45°$ polarizations, respectively. The cross-polarization radiation patterns are omitted in the figure for brevity.

B. SENSOR CHARACTERISTICS

We measured the capacitance change of the sentenna when a grounded metal plate and a human hand were brought close to the SA. Fig. 15(a) schematically depicts the setup for measuring the change in capacitance of the SE 4 at the sensor port. The measurement was performed with an LCR meter (Keysight, model E4980AL) at a test frequency of 1 MHz. Fig. 15(b) shows the results of measuring the change in capacitance of the sentenna according to the distance (d) between the sentenna and the metal plate and compares it with the simulation. As predicted in the simulation, the capacitance decreases slowly as the metal plate approaches the sentenna and then decreases rapidly as the metal plate touches the smartphone case covering the sentenna. The measured capacitance of the sentenna without the metal plate is 2.13 pF,

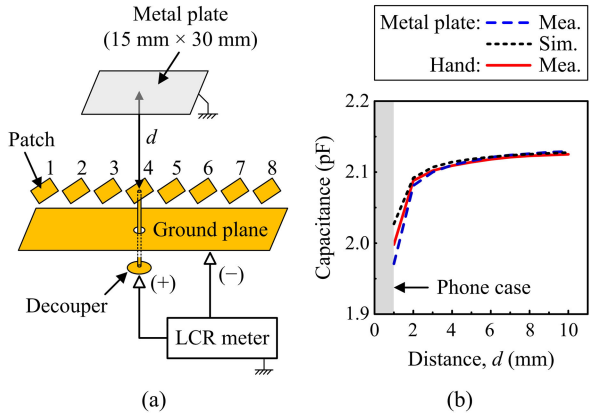

FIGURE 15. Measured capacitance change at the sensor port. (a) Measurement setup. (b) Capacitance change.

which decreases to 1.97 pF when the metal plate touches the case over the sentenna. As the capacitance is reduced by 160 fF by the metal plate, the proposed sentenna can function as a capacitive proximity sensor.

Fig. 15(b) also shows the results when a real finger is brought close to the sentenna. The measurements are nearly identical to those for the grounded metal plate. When a user's hand touches the smartphone case covering the proposed sentenna, a change in capacitance of 130 fF occurs, demonstrating that the hand grip state of the smartphone can be sensed in real time and the radiation performance of the SA can be optimized.

V. GAIN IMPROVEMENT OF SENTENNA ARRAY BASED ON HAND GRIP DETECTION

In this section, we present a simulation example in which the controller detects when the user's hand is touching an SA mounted on a smartphone and improves the gain of the SA by adjusting the amplitude of the signal supplied to each SE. Fig. 16(a) illustrates a simulation model in which a portion of the proposed SA is obscured by the user's hand (specifically the thumb). Among the eight SEs, SEs 5 to 8 are in contact with the thumb. The simulated radiation pattern at 28 GHz of each SE is depicted in Fig. 16(b), and the gain and radiation efficiency are summarized in Table 2. In this mmWave band simulation, the hand is modeled as a lossy dielectric with $\varepsilon_r = 10$ and $\tan\delta = 0.7$ [30]. The gain of SEs 5 to 8, where the thumb touches, is reduced by about 13 to 18 dB compared to SEs 1 and 2, where the thumb does not touch. This reduction occurs because the radiation efficiency decreases due to the presence of the thumb. The primary reason for this reduction in the radiation efficiency is the absorption of energy by human tissue. Additionally, due to the high dielectric constant of the thumb, the SEs become detuned and are unable to radiate normally, or the radiated waves are reflected by the thumb and absorbed into the smartphone housing, resulting in losses. Although SEs 3 and 4 are not in direct contact with the thumb, their gains are reduced compared to SEs 1 and 2 because the adjacent thumb affects their radiation efficiency.

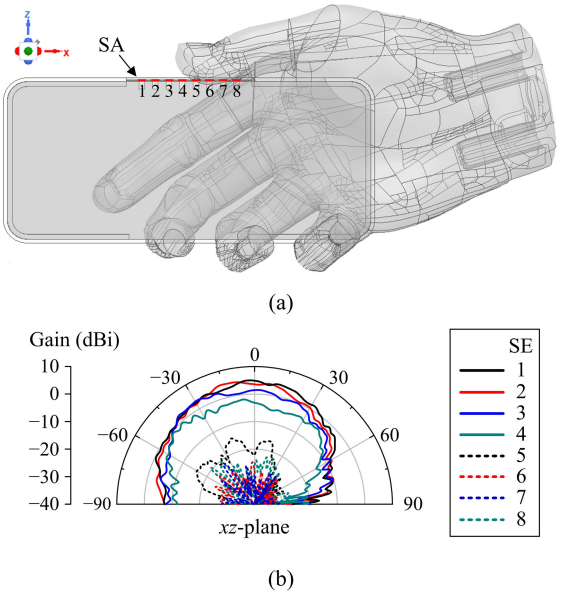

FIGURE 16. Simulation model of the user's hand effect on a smartphone. (a) Simulation model. (b) Simulated radiation patterns of SEs at 28GHz (−45° polarization).

TABLE 2. Gain, radiation efficiency, and capacitance change of SEs due to hand grip in Fig. 16(a).

SE	Gain (dBi)	Efficiency (%)	Capacitance (fF)		
			W/o hand	W/ hand	ΔC
1	5.7	64.8	2,123	2,119	−4
2	5.7	62.0	2,122	2,112	−10
3	4.2	52.4	2,124	2,109	−14
4	1.4	25.0	2,127	2,092	−35
5	−9.1	1.9	2,125	2,026	−99
6	−12.1	0.6	2,125	2,024	−102
7	−9.3	0.7	2,122	2,023	−99
8	−6.9	1.4	2,123	2,026	−97

Table 2 lists the simulation results of the capacitance of each SE with and without hands in Fig. 16(a). In this capacitance simulation, the hand is modeled as a grounded perfect electric conductor (PEC). SEs 1 to 4, which are not directly touched by the thumb, exhibit a capacitance change (ΔC) of less than 35 fF, while SEs 5 to 8, which are touched by the thumb, exhibit a change of more than 97 fF. The gain of the SA can therefore be improved by selecting SEs that are not touched by the thumb using $\Delta C = 60$ fF as an approximate threshold and supplying RF signals only to these SEs. Fig. 17 simulates and compares the radiation pattern of the SA when signals are supplied to all SEs and when signals are supplied only to SEs 1 to 4 in Fig. 16(a). Radiation patterns for five steering angles are shown and, for convenience, the radiation pattern without hands (same as Fig. 8) is also displayed. When $\theta_s = 0°$, if signals are applied to all SEs, a reduction in gain of 8.3 dB occurs due to the presence of the hand.

TABLE 3. Comparison of the mmWave mobile antennas.

Ref.	[15]	[16]	[20]	[23]	This work
Topology	1 × 4 slot	1 × 4 cavity/slot	1 × 4 slot	1 × 4 patch	1 × 8 patch
Polarization	Single	Dual (VP/HP)	Dual (−45°/+45°)	Dual (VP/HP)	Dual (−45°/+45°)
Center frequency (GHz)	39	27	27	26	28
10-dB RLBW (%)	10	19	25	23	24
Peak gain (dBi)	7.7	10.3/11.3 (VP/HP)	11.4/11.2 (−45°/+45°)	11.0/11.0 (VP/HP)	11.8/12.8 (−45°/+45°)
Volume (λ_0^3)	1.98 × 0.23 × 0.11	2.61 × 0.41 × 0.20	2.38 × 0.59 × 0.16	2.78 × 0.41 × 0.10	4.48 × 0.56 × 0.06
Height profile (λ_0)	0.11	0.20	0.16	0.10	0.06
Substrate (ε_r, tanδ)	LTCC (5.9, 0.002)	RT5880 (2.2, 0.0009)	RO4350B (3.66, 0.0037)	FR-4 (4.1−4.2, 0.03)	FR-4 (4.1, 0.03)

* All values in parameter are extracted from the measured results.

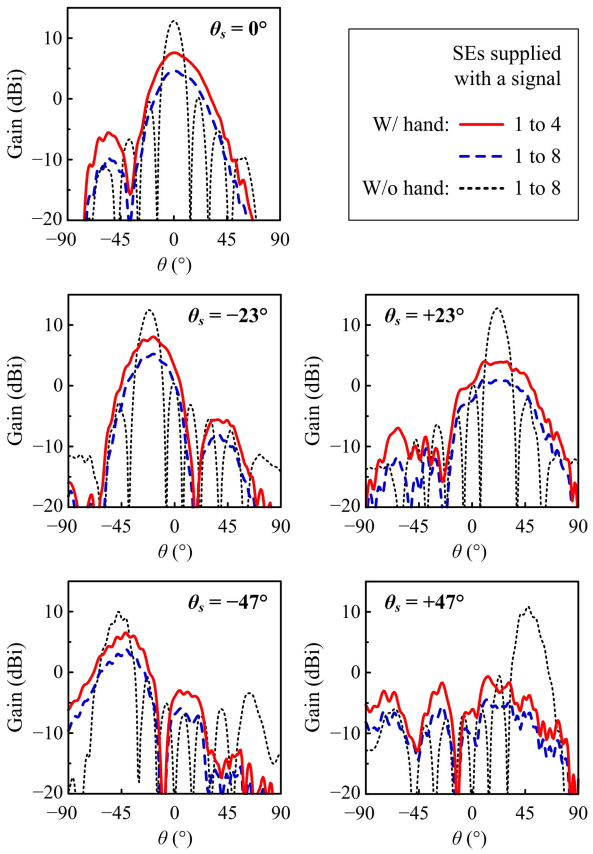

FIGURE 17. Simulated comparison of SA gains when the signal supply to the SEs changes according to the hand grip state (in the *xz*-plane at 28 GHz, −45° polarization).

However, at this time, if only the untouched SEs 1 to 4 are selected and signals are supplied, the reduction in gain is only 5.2 dB, resulting in an improvement in gain of approximately 3 dB. Similar improvements of approximately 3 dB can be achieved at other steering angles. However, at $\theta_s = +47°$, the hand obstructs the steering direction, preventing the formation of a valid main beam.

VI. CONCLUSION

In this paper, we proposed a new wideband dual-polarized patch antenna, the "sentenna," and designed a 1 × 8 phased array antenna using it. The sentenna can simultaneously function as an antenna and a proximity sensor without mutual interference, making it effectively applicable to an adaptive phased array antenna system capable of real-time compensation for performance degradation due to the effects of user hands in 5G smartphones. Table 3 summarizes the performance comparison of the proposed sentenna with recently reported mmWave mobile antennas. The presented sentenna is built with the lowest height profile using the least expensive substrate among the listed works. Nevertheless, the sentenna's gain and bandwidth are comparable to those of other antennas. The proximity sensor feature also significantly enhances the sentenna's usability.

REFERENCES

[1] T. S. Rappaport, S. Sun, R. Mayzus, H. Zhao, Y. Azar, K. Wang, G. N. Wong, J. K. Schulz, M. Samimi, and F. Gutierrez, "Millimeter wave mobile communications for 5G cellular: It will work!" *IEEE Access*, vol. 1, pp. 335–349, 2013.

[2] W. Hong, Z. H. Jiang, C. Yu, D. Hou, H. Wang, C. Guo, Y. Hu, L. Kuai, Y. Yu, Z. Jiang, Z. Chen, J. Chen, Z. Yu, J. Zhai, N. Zhang, L. Tian, F. Wu, G. Yang, Z.-C. Hao, and J. Y. Zhou, "The role of millimeter-wave technologies in 5G/6G wireless communications," *IEEE J. Microw.*, vol. 1, no. 1, pp. 101–122, Jan. 2021.

[3] M. Agiwal, A. Roy, and N. Saxena, "Next generation 5G wireless networks: A comprehensive survey," *IEEE Commun. Surveys Tuts.*, vol. 18, no. 3, pp. 1617–1655, 3rd Quart., 2016.

[4] D. Liu, X. Gu, C. W. Baks, and A. Valdes-Garcia, "Antenna-in-package design considerations for Ka-band 5G communication applications," *IEEE Trans. Antennas Propag.*, vol. 65, no. 12, pp. 6372–6379, Dec. 2017.

[5] X. Gu, D. Liu, C. Baks, O. Tageman, B. Sadhu, J. Hallin, L. Rexberg, P. Parida, Y. Kwark, and A. Valdes-Garcia, "Development, implementation, and characterization of a 64-element dual-polarized phased-array antenna module for 28-GHz high-speed data communications," *IEEE Trans. Microw. Theory Techn.*, vol. 67, no. 7, pp. 2975–2984, Jul. 2019.

[6] Q. Yang, S. Gao, Q. Luo, L. Wen, Y.-L. Ban, X.-X. Yang, X. Ren, and J. Wu, "Cavity-backed slot-coupled patch antenna array with dual slant polarization for millimeter-wave base station applications," *IEEE Trans. Antennas Propag.*, vol. 69, no. 3, pp. 1404–1413, Mar. 2021.

[7] W. Hong, "Solving the 5G mobile antenna puzzle: Assessing future directions for the 5G mobile antenna paradigm shift," *IEEE Microw. Mag.*, vol. 18, no. 7, pp. 86–102, Nov. 2017.

[8] W. Hong, K.-H. Baek, and S. Ko, "Millimeter-wave 5G antennas for smartphones: Overview and experimental demonstration," *IEEE Trans. Antennas Propag.*, vol. 65, no. 12, pp. 6250–6261, Dec. 2017.
[9] A. H. Naqvi and S. Lim, "Review of recent phased arrays for millimeter-wave wireless communication," *Sensors*, vol. 18, no. 10, p. 3194, Sep. 2018.
[10] W. Hong, K.-H. Baek, Y. Lee, Y. Kim, and S.-T. Ko, "Study and prototyping of practically large-scale mmWave antenna systems for 5G cellular devices," *IEEE Commun. Mag.*, vol. 52, no. 9, pp. 63–69, Sep. 2014.
[11] W. El-Halwagy, R. Mirzavand, J. Melzer, M. Hossain, and P. Mousavi, "Investigation of wideband substrate-integrated vertically-polarized electric dipole antenna and arrays for mm-wave 5G mobile devices," *IEEE Access*, vol. 6, pp. 2145–2157, 2018.
[12] I.-J. Hwang, B. Ahn, S.-C. Chae, J.-W. Yu, and W.-W. Lee, "Quasi-Yagi antenna array with modified folded dipole driver for mmWave 5G cellular devices," *IEEE Antennas Wireless Propag. Lett.*, vol. 18, pp. 971–975, 2019.
[13] H. Li, Y. Li, L. Chang, W. Sun, X. Qin, and H. Wang, "A wideband dual-polarized endfire antenna array with overlapped apertures and small clearance for 5G millimeter-wave applications," *IEEE Trans. Antennas Propag.*, vol. 69, no. 2, pp. 815–824, Feb. 2021.
[14] J. Seo, I. Yoon, J. Jung, J. Ryoo, J. Park, W. Lee, D. Ko, and J. Oh, "Miniaturized dual-band broadside/endfire antenna-in-package for 5G smartphone," *IEEE Trans. Antennas Propag.*, vol. 69, no. 12, pp. 8100–8114, Dec. 2021.
[15] J. Park, H. Seong, Y. N. Whang, and W. Hong, "Energy-efficient 5G phased arrays incorporating vertically polarized endfire planar folded slot antenna for mmWave mobile terminals," *IEEE Trans. Antennas Propag.*, vol. 68, no. 1, pp. 230–241, Jan. 2020.
[16] L. Sun, Y. Li, and Z. Zhang, "Wideband dual-polarized endfire antenna based on compact open-ended cavity for 5G mm-wave mobile phones," *IEEE Trans. Antennas Propag.*, vol. 70, no. 3, pp. 1632–1642, Mar. 2022.
[17] S. Islam, M. Zada, and H. Yoo, "Highly compact integrated sub-6 GHz and millimeter-wave band antenna array for 5G smartphone communications," *IEEE Trans. Antennas Propag.*, vol. 70, no. 12, pp. 11629–11638, Dec. 2022.
[18] J.-U. Yoo and H.-W. Son, "5G mmWave patch antenna array with proximity sensing function for detecting user's hand grip on mobile terminals," *Electron. Lett.*, vol. 59, no. 7, Apr. 2023, Art. no. e12769.
[19] J.-U. Yoo, J.-M. Kim, D. Im, and H.-W. Son, "Dual polarized patch antenna array with capacitive proximity sensor for hand grip detection in 5G mmWave mobile devices," in *SBMO/IEEE MTT-S Int. Microw. Optoelectronics Conf. (IMOC)*, Castelldefels, Spain, Nov. 2023, pp. 88–90.
[20] X. Xia, C. Yu, F. Wu, Z. H. Jiang, Y.-L. Li, Y. Yao, and W. Hong, "Millimeter-wave phased array antenna integrated with the industry design in 5G/B5G smartphones," *IEEE Trans. Antennas Propag.*, vol. 71, no. 2, pp. 1883–1888, Feb. 2023.
[21] W. Hong, K.-H. Baek, and A. Goudelev, "Multilayer antenna package for IEEE 802.11ad employing ultralow-cost FR4," *IEEE Trans. Antennas Propag.*, vol. 60, no. 12, pp. 5932–5938, Dec. 2012.
[22] W. Hong, K.-H. Baek, and A. Goudelev, "Grid assembly-free 60-GHz antenna module embedded in FR-4 transceiver carrier board," *IEEE Trans. Antennas Propag.*, vol. 61, no. 4, pp. 1573–1580, Apr. 2013.
[23] G. Kim and S. Kim, "Design and analysis of dual polarized broadband microstrip patch antenna for 5G mmWave antenna module on FR4 substrate," *IEEE Access*, vol. 9, pp. 64306–64316, 2021.
[24] B. Yu, K. Yang, C.-Y.-D. Sim, and G. Yang, "A novel 28 GHz beam steering array for 5G mobile device with metallic casing application," *IEEE Trans. Antennas Propag.*, vol. 66, no. 1, pp. 462–466, Jan. 2018.
[25] A. Alammouri, J. Mo, B. L. Ng, J. C. Zhang, and J. G. Andrews, "Hand grip impact on 5G mmWave mobile devices," *IEEE Access*, vol. 7, pp. 60532–60544, 2019.
[26] F. Fernandes, C. Rom, J. Harrebek, S. Svendsen, and C. N. Manchón, "Hand blockage impact on 5G mmWave beam management performance," *IEEE Access*, vol. 10, pp. 106033–106049, 2022.
[27] J. M. Kim, H. W. Son, and D. G. Im, "Phased array antenna module and mobile device including same," U.S. Patent 12 003 028, Jun. 4, 2024.
[28] Z. Chen and R. C. Luo, "Design and implementation of capacitive proximity sensor using microelectromechanical systems technology," *IEEE Trans. Ind. Electron.*, vol. 45, no. 6, pp. 886–894, Dec. 1998.
[29] C. B. Thoresen and U. Hanke, "Numerical simulation of mutual capacitance touch screens for ungrounded objects," *IEEE Sensors J.*, vol. 17, no. 16, pp. 5143–5152, Aug. 2017.
[30] S. S. Zhekov, O. Franek, and G. F. Pedersen, "Dielectric properties of human hand tissue for handheld devices testing," *IEEE Access*, vol. 7, pp. 61949–61959, 2019.

JEONG-UNG YOO received the B.S. degree in electronics engineering and the M.S. and Ph.D. degrees in electronics and information engineering from Jeonbuk National University, Jeonju, South Korea, in 2016, 2018, and 2023, respectively. He is currently with the Agency for Defense Development, Daejeon, South Korea. His research interests include wideband antennas, millimeter-wave antenna arrays, and orbital angular momentum.

JUNG-MU KIM (Member, IEEE) was born in Jeonju, South Korea, in 1977. He received the B.S. degree in electronic engineering from Ajou University, Suwon, South Korea, in 2000, and the M.S. and Ph.D. degrees in electrical engineering and computer science from Seoul National University, Seoul, South Korea, in 2002 and 2007, respectively. From 2007 to 2008, he was a Postdoctoral Fellow at the University of California, San Diego. In 2008, he joined the Faculty of the Division of Electronic Engineering, Jeonbuk National University, where he is currently a Full Professor. His research interests include the IMU, SPR sensor, RF MEMS for 5G and ink-jet printing, and 3-D printing-based printed electronics.

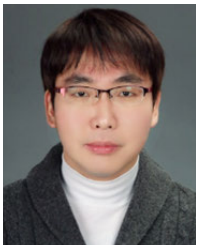

DONGGU IM (Member, IEEE) received the B.S., M.S., and Ph.D. degrees in electrical engineering and computer science from Korea Advanced Institute of Science and Technology (KAIST), Daejeon, South Korea, in 2004, 2006, and 2012, respectively. From 2012 to 2013, he was a Postdoctoral Researcher with KAIST, where he was involved in the development of the first RF SOI CMOS technology in Korea with the National NanoFab Center (NNFC), SOI Business Team, Daejeon. In 2013, he joined the Texas Analog Center of Excellence (TxACE), Department of Electrical Engineering, University of Texas at Dallas, as a Research Associate. In 2014, he joined the Division of Electronic Engineering, Jeonbuk National University, South Korea, where he is currently an Associate Professor. His research interests include CMOS analog/RF/mmwave ICs and system design for wireless communications.

HAE-WON SON (Member, IEEE) received the B.S. degree in electronics engineering from Kyungpook National University, Daegu, South Korea, in 1994, and the M.S. and Ph.D. degrees in electrical engineering from Korea Advanced Institute of Science and Technology (KAIST), Daejeon, South Korea, in 1996 and 2001, respectively. From 1996 to 2003, he was with Samsung Electronics, Suwon, South Korea. From 2003 to 2007, he was with the Electronics and Telecommunications Research Institute (ETRI), Daejeon. In 2007, he joined as a Faculty Member with Jeonbuk National University, Jeonju, South Korea, where he is currently a Full Professor. His research interests include antennas and propagation, RF/microwave circuits, and RFID/ubiquitous sensor networks.